Composite Structures 160 (2017) 23–35

Contents lists available at ScienceDirect

Composite Structures

journal homepage: www.elsevier.com/locate/compstruct

Load bearing and failure characteristics of perforated square CFRP tubes under axial crushing

Qiang Liu [a,b,*], Jingbo Ma [a], Xiyu Xu [a], Yinghan Wu [a], Qing Li [c]

[a] School of Engineering, Sun Yat-Sen University, Guangzhou City 510006, China
[b] State Key Laboratory of Advanced Design and Manufacture for Vehicle Body, Hunan University, Changsha 410082, China
[c] School of Aerospace, Mechanical and Mechatronic Engineering, University of Sydney, Sydney, NSW 2006, Australia

ARTICLE INFO

Article history:
Received 17 June 2016
Revised 28 September 2016
Accepted 12 October 2016
Available online 13 October 2016

Keywords:
Perforated
CFRP
Crashworthiness
Bladder molding
Cutout

ABSTRACT

Open holes or cutouts have been commonly used in composite structures for various engineering purposes. This paper aims to investigate the load bearing behavior and failure characteristics of the square weave carbon fiber reinforced plastic (CFRP) tubes with open holes subjected to axial compression. Effects of hole size, hole shape and hole distribution on failure modes and mechanical behaviors were evaluated experimentally and numerically. Different with the progressive crushing mode seen in the intact CFRP tubes, mid-height collapse and unstable local buckling were observed in the axial crushing tests. The peak load and specific energy absorption (SEA) of the perforated tubes decreased by around 3–22% and 26–57%, respectively, compared to those of the intact CFRP counterparts. It was found that the effect of hole size on failure strength in tubes was less sensitive than that in perforated composite laminates, but was relatively stronger than the perforation shape and distribution. The damage mechanisms were explored in-depth using strain gauge tests and finite element analysis, which showed a significant increase in shear stress around the holes prior to final failure.

1. Introduction

Carbon fiber reinforced plastic (CFRP) has been widely used in various engineering structures attributable to its advantages of specific stiffness and energy absorption capability over metallic materials [1,2]. Engineering design often requires structural discontinuities such as open holes or cutoffs for connection, joint and access. The presence of holes interrupted the continuous distributions of stress and strain within the panels, potentially causing significant stress concentration around the holes and leading to considerable reduction in load bearing capacities [3,4]. Therefore, the influence and sensitivity of open holes on structural behaviors signify a critical issue in practice.

Early work in the area, as summarized by Awerbuch and Madhukar [5], largely focused the studies of perforated composite laminates (plates) on initiation of crack tip, damage zone for critical crack tip, sensitivity of hole, fracture toughness, failure modes from the microscopic and macroscopic aspects. For example, Guynn and Bradley [6] comprehensively investigated the micromechanics of compressive failure of the composite laminates with open hole; and they found that the damage zone was initiated at the edges of the hole by local buckling and/or shear crippling, then stably propagated until reached a critical size. Soutis et al. [7–9] revealed that the compressive failure of the perforated laminate was governed by plastic microbuckling of 0° plies. Starnes [10] carried out an experimental study on the failure characteristics of compressively-loaded graphite-epoxy components; and found that the stress concentrations near holes reduced the compressive strength of strength-critical laminates.

It has been recognized that the failure strength of perforated laminates decreased as the increase in hole size [11–13]. Hallett et al. [14] investigated the effect of hole size on the tensile strength of composite laminates containing circular holes; and they showed that there was a large difference in failure stress and mechanism due to changes in hole diameter, ply and laminate thickness. Rezaeepazhand and Jafari [15] undertook an analytical study on the effects of hole shapes on the load bearing capacity and stress concentration of composite plates subjected to a uni-axial tension. Kumar and Singh [16] explored the stability and failure of a composite laminate with a centrally placed hole in different shapes, such as circular, square, diamond, elliptical-vertical and elliptical-horizontal openings under combined application of uni-axial compression and in-plane shear loads. Durelli et al. [17,18], Muc [19] and Liu et al. [20] attempted to optimize the hole shape for

* Corresponding author at: School of Engineering, Sun Yat-Sen University, Guangzhou City 510006, China.
E-mail address: liu5168198110@126.com (Q. Liu).

http://dx.doi.org/10.1016/j.compstruct.2016.10.032
0263-8223/

minimizing stress concentration. It was found that the optimized hole reduced the stress concentration factor by as much as 21% compared with a circular hole [17].

Furthermore, there have been some studies on finite element analysis (FEA) of composite structures with holes. Ng et al. [21] carried out a micromechanical three-dimensional finite element analysis for the 2/2 twill weave T300 carbon/epoxy woven fabric composite laminates with drilled circular holes in different sizes using ANSYS code; and they revealed that the location of failure initiation for laminates with large hole size differed from those with smaller holes. Su et al. [22] proposed a progressive damage model using the ABAQUS UMAT code for open-hole composite laminates under compressive loading; and they further applied it to study the size effects. Wang et al. [23] conducted an experimental and numerical investigation into the compressive strength of intact and perforated quasi-isotropic laminates; and they demonstrated that progressive damage approach was fairly accurate and efficient for predicting the structural strength with open-hole using ABAQUS. Xu et al. [24] exhibited that the cohesive zone model was able to predict the strengths of perforated structural samples and the predictive accuracy of the strength was within 10%.

Note that the compressive responses of perforated composite tubes have drawn increasing attention for their theoretical and practical significance. For example, Taheri-Behrooz et al. [25] examined the responses of the perforated E-glass/epoxy tube subjected to axial compressive loading; and they found that the perforated tubes exhibited similar instability mode to the intact tubes, but the critical load and stiffness of the perforated tube were considerably lower. Wang et al. [26] investigated the influences of various parameters on the compressive behaviors of perforated glass fiber reinforced polymer (GFRP) circular tubes; and they found that the axial stiffness, critical load and deformation capacity of perforated tubes decreased substantially. Even with these reports, the perforated composite tubes have been under-studied compared with the laminate counterparts. More specifically, evaluations on the load bearing capacity and failure characteristics of the perforated CFRP square tubes have been far inadequate. As a matter of

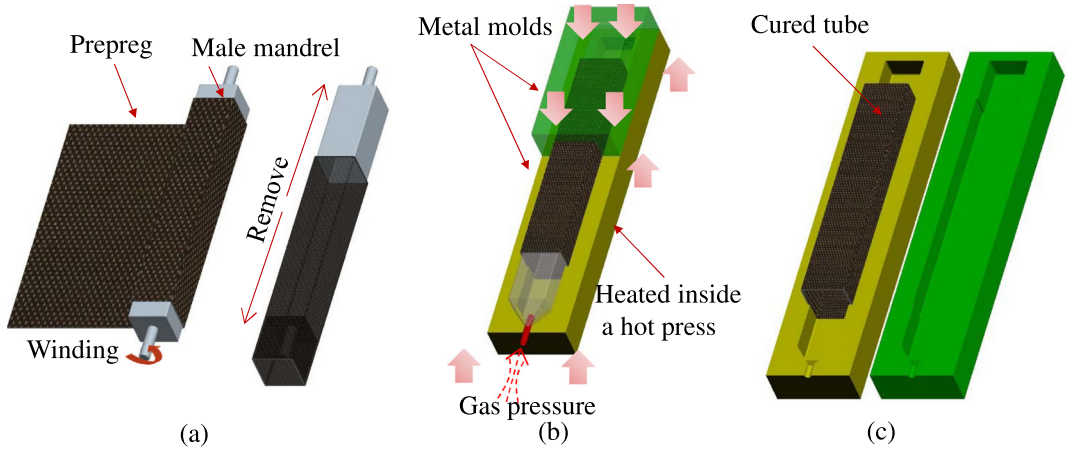

Fig. 1. Schematic of fabrication process: (a) filament winding prepreg, (b) curing inside a hot press and (c) cured specimen.

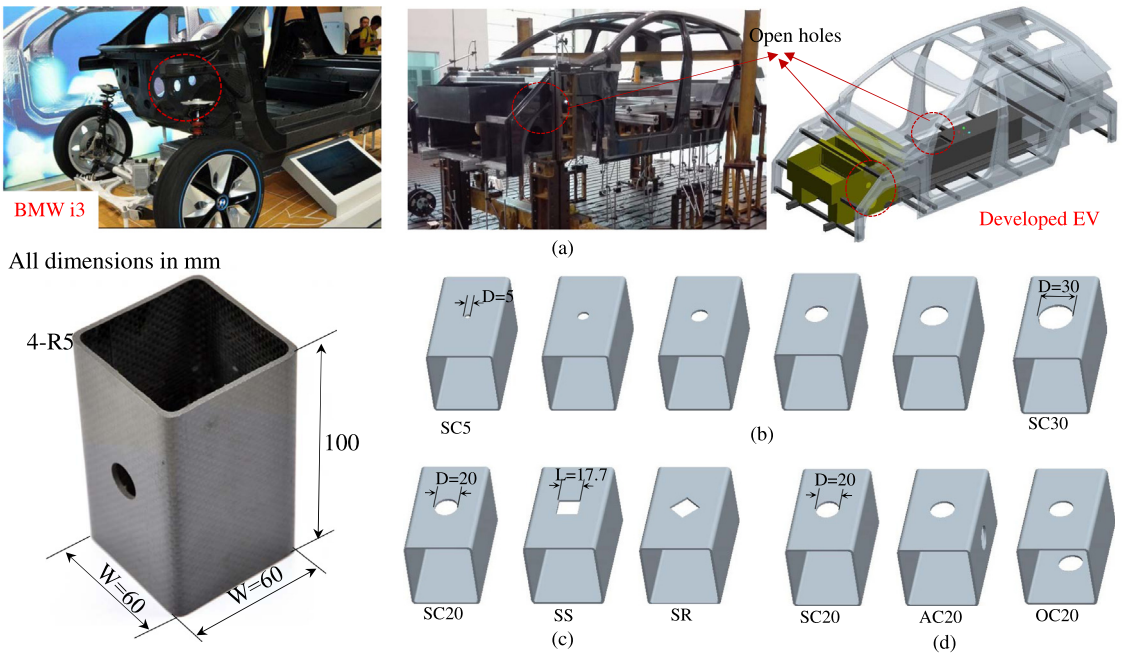

Fig. 2. Schematic of tested specimens and geometric features of perforation.

fact, CFRP tubes are increasingly utilized in body frames in advanced lightweight structures, such as BMW electric vehicles and Lexus LFA vehicles [27,28], placing growing significance and urgency to systematically understand its failure mechanism and crashworthiness.

This study aims to gain a comprehensive understanding of the influence of the perforating configuration on load bearing behavior and failure characteristics of the CFRP square tubes. In this paper, the typical load-displacement curves and failure modes are identified first; the effects of hole size (i.e. the diameter of 5, 10, 15, 25 and 30 mm in the circular hole), hole shape (circular, square and rhombus) and hole distribution (single face, opposite faces and adjacent faces) on load bearing capacity and energy absorption are explored in detail. The differences in the crushing responses between the perforated and intact tubes are quantified for comparison. The strain gauges test and finite element analysis in LS-DYNA

Table 1
Geometry and crushing characteristics of tested tubes.

Specimen label	Thickness (mm)	Length (mm)	Mass (1×10^{-3} kg)	Crushing distance (mm)	Failure mode	Peak load (kN)	Mean load (kN)	SEA (kJ/kg)
NH-1	1.99	100	73.51	80		99.81	62.74	85.53
NH-2	2.01	100	73.48	80		100.32	54.72	74.73
NH-3	2.00	100	73.60	80		98.52	62.57	85.21
Mean	2.00	100	73.53			99.55	60.01	81.82
S.D.	0.01		0.05			0.76	3.74	5.02
SC5-1	2.00	100	74.57	80	II	94.93	40.28	52.51
SC5-2	2.01	100	75.29	80	II	98.46	34.74	46.74
SC5-3	2.01	100	74.94	80	I	97.26	24.15	31.55
Mean	2.01	100	74.93			96.88	33.06	43.60
S.D.	0.00		0.29			1.47	6.69	8.84
SC10-1	1.99	100	74.84	80	II	92.99	54.66	70.41
SC10-2	2.00	100	74.37	80	I	95.69	34.54	45.36
SC10-3	2.00	100	71.58	80	I	92.68	37.33	50.95
Mean	2.00	100	73.60			93.79	42.18	55.57
S.D.	0.00		1.44			1.35	8.90	10.74
SC15-1	2.01	100	71.94	80	I	83.37	47.01	62.98
SC15-2	2.01	100	71.90	80	I	81.82	34.79	47.01
SC15-3	2.00	100	74.45	80	I	91.21	46.31	59.88
Mean	2.01	100	72.76			85.47	42.70	56.62
S.D.	0.00		1.19			4.11	5.60	6.91
SC20-1	1.99	100	72.20	80	I	79.84	16.98	23.18
SC20-2	2.00	100	72.40	80	I	85.22	29.25	39.48
SC20-3	2.01	100	72.25	80	I	77.16	31.38	43.03
Mean	2.00	100	72.28			80.74	25.87	35.23
S.D.	0.01		0.08			3.35	6.35	8.64
SC25-1	2.01	100	71.64	80	I	77.72	36.09	50.38
SC25-2	2.01	100	71.82	80	I	82.60	39.36	54.80
SC25-3	2.00	100	71.35	80	I	80.20	38.12	53.42
Mean	2.01	100	71.60			80.17	37.86	52.87
S.D.	0.00		0.19			1.99	1.35	1.85
SC30-1	1.99	100	71.56	80	I	81.84	45.35	63.37
SC30-2	2.00	100	71.28	80	I	73.97	41.63	58.40
SC30-3	2.01	100	71.88	80	I	77.72	43.26	60.18
Mean	2.00	100	71.57			77.84	43.41	60.65
S.D.	0.01		0.25			3.21	1.52	2.06
AC20-1	2.00	100	71.15	80	I	87.81	33.95	47.36
AC20-2	2.00	100	71.31	80	I	80.09	31.96	43.48
AC20-3	2.00	100	71.29	80	I	74.77	40.44	56.43
Mean	2.00	100	71.25			80.89	35.45	49.09
S.D.	0.00		0.07			5.35	3.62	5.43
OC20-1	2.00	100	71.34	80	I	74.66	42.06	57.30
OC20-2	1.99	100	71.76	80	I	85.47	43.79	59.29
OC20-3	2.00	100	71.29	80	I	76.67	24.01	32.79
Mean	2.00	100	71.46			78.93	36.62	49.79
S.D.	0.00		0.21			4.69	8.94	12.05
SS-1	1.99	100	71.33	80	I	87.63	25.86	35.09
SS-2	2.00	100	71.32	80	I	90.49	45.47	61.49
SS-3	2.01	100	72.21	80	I	80.49	34.18	45.71
Mean	2.00	100	71.62			86.20	35.17	47.43
S.D.	0.01		0.42			4.21	8.04	10.85
SR-1	2.01	100	72.00	80	I	80.85	32.01	43.42
SR-2	2.00	100	71.80	80	I	85.48	37.53	50.69
SR-3	2.01	100	69.56	80	I	76.42	39.12	52.60
Mean	2.01	100	71.12			80.92	36.22	48.90
S.D.	0.00		1.11			3.70	3.05	3.95

Note that the specimen label, e.g. SC5-1, represents the distribution of single face, circular hole with a diameter of 5 mm in Specimen #1 of this group; NH, represents no hole (intact); S.D. denotes the standard deviation of tested specimens; Mode I and II represent the failure mode of mid-height collapse and unstable buckling, respectively.

are also carried out to further understand the damage mechanism as well as initiation and propagation of the cracks in the perforated tubal CFRP structures.

2. Materials and methods

2.1. Sample preparation

The Toray plain weave carbon fiber T300/epoxy prepreg was chosen to fabricate the square tube. The fiber volume fraction was around 56%. The average tensile strength and Young's modulus, determined from the in-house tests on the 6-ply laminates according to ASTM D3039-76, was 590 MPa and 56 GPa, respectively [29]. The CFRP square tubes were fabricated using the bladder molding process, which consisted of preparing carbon and resin preform, placing into a metal mold, exerting pressure from the inside with an inflatable bladder and curing within a hot press [30], as illustrated in Fig. 1. The prepreg was first winded over a male mandrel under tension until reaching the desired ply number of 9; then the mandrel was removed, leaving the smooth preform

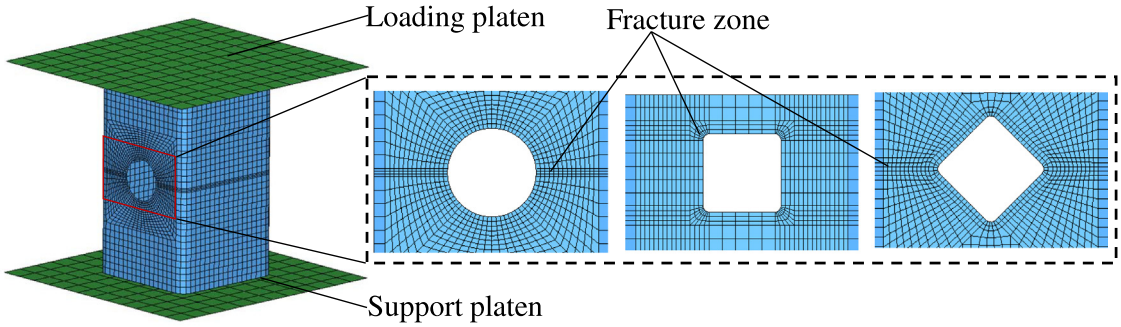

Fig. 3. Schematic of finite element model.

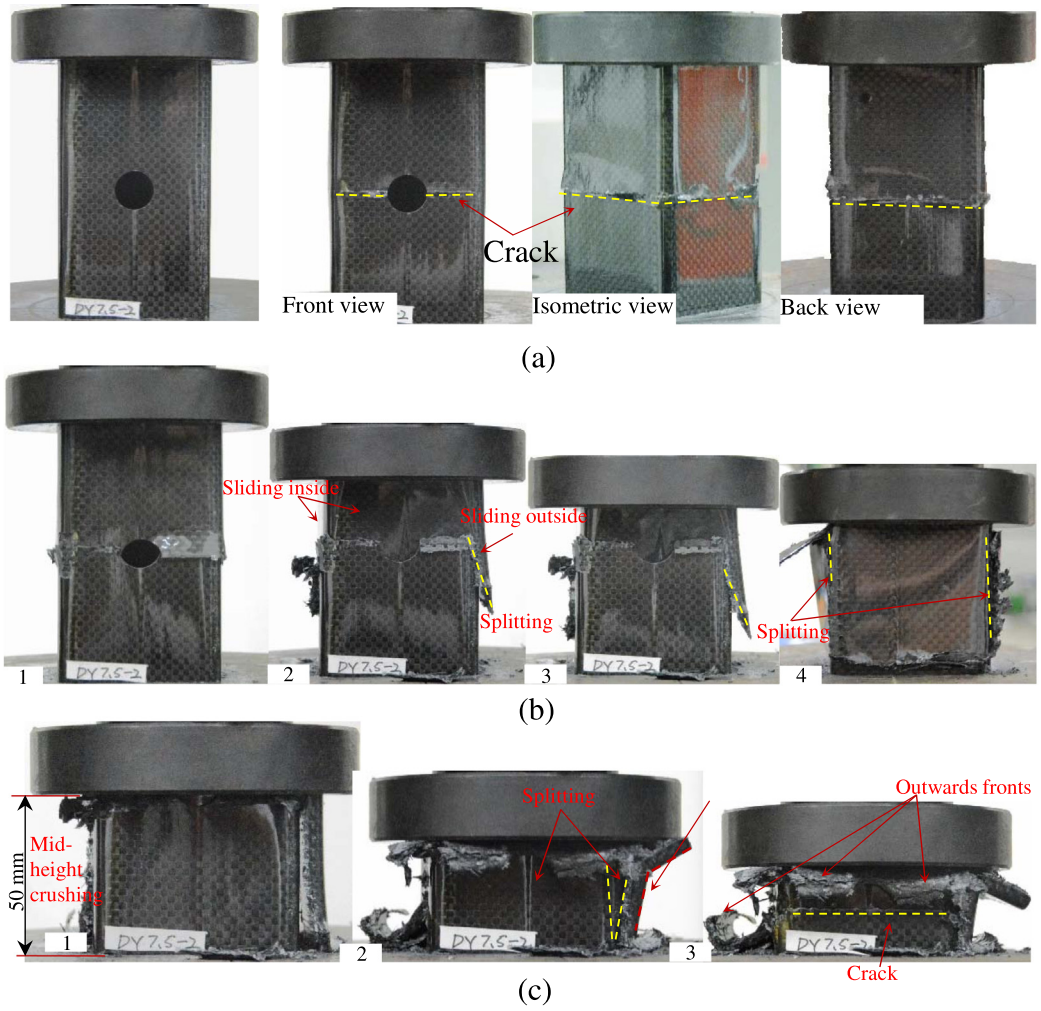

Fig. 4. Failure mode I: (a) crack initiation and propagation, (b) sliding of separated walls and (c) second load climbing.

with uniform thickness. The preform was filled with the thin thermoplastic film bladder and placed smoothly into the metal mold. The closed molds were heated up to around 150 °C inside a hot press, and a pressure of 1.25 MPa was applied in the bladder to load the preforms into molds. Then the fabricated tube was cured for about 45 min to yield an optimum strength and hardness. The desired length of specimens (100 mm) was sectioned from the cured tubes (350 mm); both of the two ends were machined to flat, without placing trigger features. Finally, the desired holes with different diameters, shapes and distributions were drilled in the middle of flat tubal wall using a tungsten carbide compact bit within a high speed computer numerical control (CNC) milling machine to minimize fiber damage and delamination around the hole edge.

2.2. Geometry of specimens

There has been intensifying interest in the use of composite materials for the design of lightweight structure of vehicle in the recent years, particular in the body structures of electric vehicles, such as BMW i 3 and our recently developed lightweight EVs (as shown in Fig. 2a). While the best effort we have made to avoid open holes, there is inevitably need of cutouts for the access to drive shaft, control units and so on. The tubal specimens were prepared as a basic component to generate fundamental data for understanding the effects of geometrical and distributional features of perforation on the crushing characteristics of CFRP component.

Based upon the design requirements of open holes in the novel electric vehicle body as developed in [31], three sets of different perforation features were investigated herein: (1) the diameters of circular hole with 5, 10, 15, 20, 25, and 30 mm (Fig. 2b); (2) the shapes of holes in square, circle and rhombus (Fig. 2c); and (3) the distributions of holes in single face, adjacent faces and opposite faces (Fig. 2d). The specific specimen geometry and test results of these specimens were summarized in Table 1.

2.3. Testing procedure

The quasi-static axial crushing tests were performed at room temperature in a Sans 5205 digitalized testing machine with a loading capacity of 200 kN. The specimen was placed in between the loading platen and support platen; and loaded at a constant rate of 2 mm/min. Load and displacement data were recorded directly in the automatic data acquisition system. The strain gauges were also used to record the strain data around the hole. The peak load, mean load and specific energy absorption (SEA) were then calculated based upon the load-displacement curve.

2.4. Finite element analysis

Finite element analysis was performed to model the crack initiation and propagation in the perforated tubes, which was typically difficult to observe in detail experimentally. Fig. 3 exemplifies the FEA models of the CFRP tubes with the circular, rhombus and square cutouts, respectively. In these FEA models, the lower support platen was defined as a fixed rigid shell; and the upper loading platen was defined as a moving rigid shell with the same velocity as that in the experiment. A single layer of four-node, fully integrated, shell elements (Type 16 in LS-DYNA) was used to model the tubal walls.

The material model 54 "mat_enhanced_composite damage" [32], one of the most commonly-used material available for composites in LS-DYNA, was selected to model the material behaviors of composite tubes. The damage model, valid for thin shell elements, is based upon the Chang-Chang failure criterion [33], which allows users to input any orthotropic properties by specifying local material axes and appropriate constitutive constants [34]. The failure parameters used in the numerical study were mostly from our in-house experiments as well as other literatures [34–36].

Three different contact algorithms, namely, Automatic_surface_to_surface, Automatic_single_surface and Automatic_nodes_to_surface, were used here to model the interactions between contacting parts (as illustrated in Fig. 3). A master-surface to slave-node contact was defined between the support platen and the nodes of tubes (Automatic_nodes_to_surface); and the contact of surface in the top end of tube to the upper platen was defined as Automatic_surface_to _surface. All the finite element (FE) models used the Automatic_single_surface to prevent self-penetration of the deformed tubal surface.

The FE mesh was determined by considering the computational cost and local refinement around the cutout edge through a mesh convergence test in this study. Overall, the mesh size was set

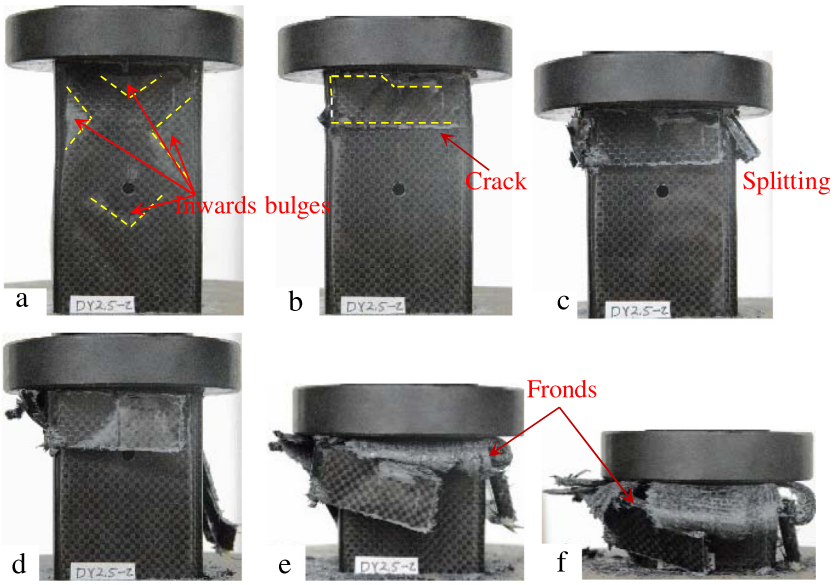

Fig. 5. Crushing process of failure mode II.

approximately uniformly, about 0.5–1 mm along the fracture zone and approximate 3 mm in the non-critical regions, as shown in Fig. 3. A sufficient number of elements was placed in the front of a predicted crack tip [22,37]. The loading procedure, boundary conditions, material properties and tube geometry in the FE models were set as consistent with the experimental conditions as possible.

3. Results and discussion

3.1. Failure modes

Unlike the failure mode of progressive end crushing seen in the previous studies on the crushing tests of the intact CFRP tubes [30,38], two unstable failure modes, classified as mid-height collapse (mode I) and unstable local buckling (mode II), were observed in the tests of the perforated CFRP tubes. Details on the failure modes corresponding to each specimen are summarized in Table 1.

Mode I is characterized by mid-height collapse along the circumference of the tube walls which was observed in approximately 81.8% of all the tested tubes, with relatively big hole (D/C >4.0%, D: hole diameter; C: tubal transverse circumference). As shown in Fig. 4, three stages could be distinguished in the crushing process: the first stage corresponded to the crack initiation and propagation along the wall (Fig. 4a); the second corresponded to sliding of the fractured upper and lower halves (Fig. 4b); and the third corresponded to the second load climbing after the two halves contacted with the loading and support platens (Fig. 4c).

The mid-height collapse was initiated at a critical peak load when the displacement of the loading platen was typically less than 5% of whole crushing distance. It is noted that the peak load of perforated tube was lower than that of the intact tube (Table 1), which agreed well with the sizeable reduction in strength observed in the perforated laminates due to the presence of strong stress concentration [8]. Circumferential cracks occurred from the hole edges and expanded radically along the circumference of the tube walls until they joined together in the opposite wall, splitting the tube into two separated halves. This stage corresponded to a significant drop of the compressive load (reduced by approximately 87% from the peak load) and a crisp sound. Subsequently, the upper half of the tube started penetrating the lower half, causing further unstable collapse and splitting at the corners of the tubal shell. The fractured upper wall segments slid inside and outside of the lower half of the tube until the crushing displacement approximately reached to the half of the tube length (Fig. 4b). After the two halves contacted to the loading and support platens, both parts of the fractured shell started resisting further compression, leading to an immediate increase in the compressive load and forming the second loading peak (Fig. 4c).

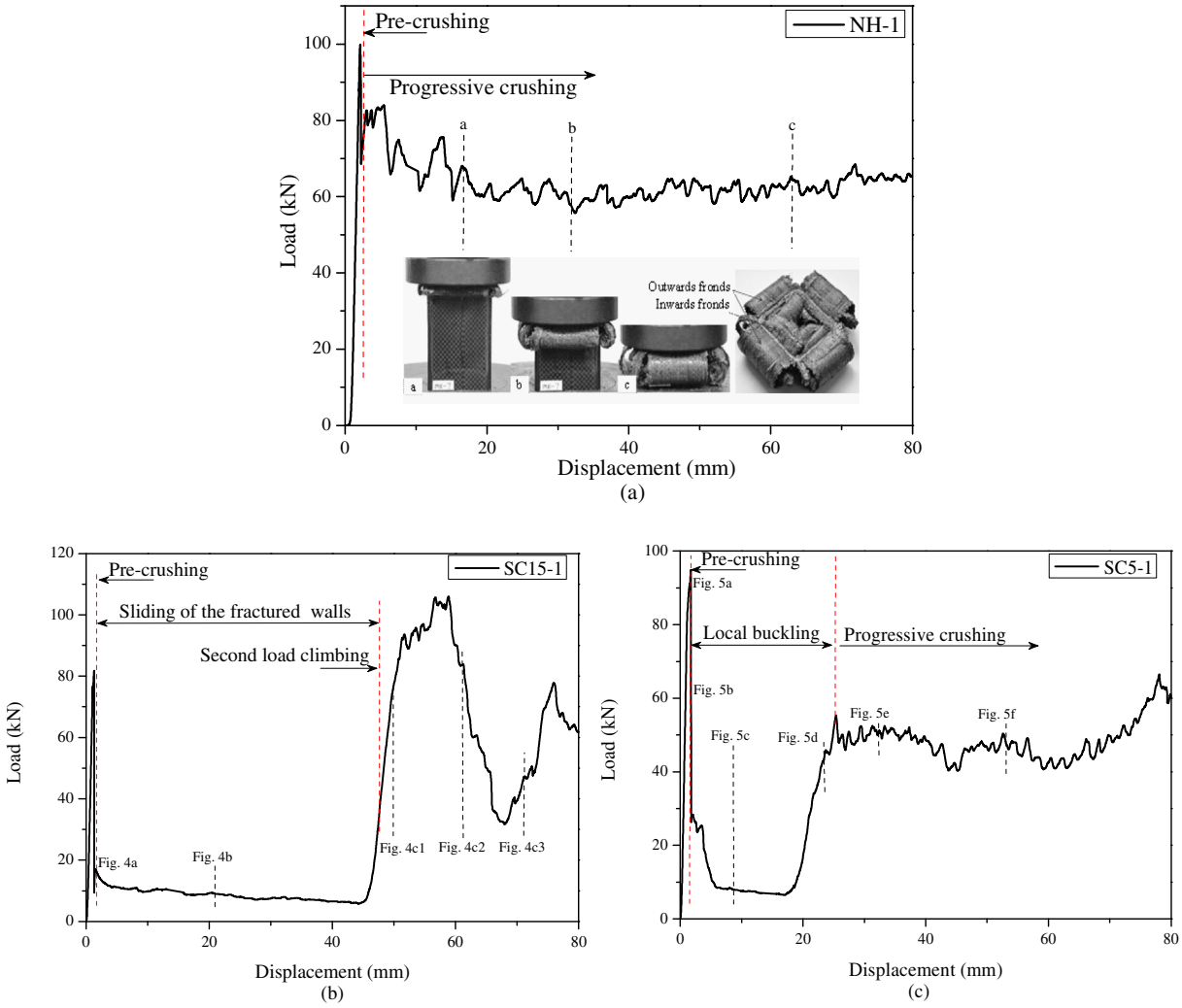

Fig. 6. Typical load-displacement curves: (a) progressive crushing, (b) mode I and (c) II.

Mode II represents the collapse characterized by the local buckling in one end of the tube which corresponded to the "unstable local buckling" as depicted in [30,38]. This failure mode was observed in the case of tube SC5 and SC10 (c.f. Table 1) with a small hole (D/C <4.0%). It is noted that the tested tube presented the local buckling first and then the progressive folding as described by Liu et al. [30] and Mamalis et al. [38].

Failure mode II was also initiated at the end of elastic phase that corresponded to the first peak load, featured with several inwards bulges occurring on the tube wall due to the local stress concentrations (Fig. 5a). It was immediately followed by the fracture of matrix and reinforced fiber with significant reduction in the load. As deformation proceeded, a crack initiated at the severe buckling region and grew along the circumference of the tube perpendicular to the loading direction (Fig. 5b and c). Subsequently the tube was separated by the growing crack into two parts, and the upper part was split at the tube corners and slid outwards under compression until the lower part contacted with loading platen and started folding progressively (Fig. 5e and f).

3.2. Load-displacement curve

Fig. 6 plots the typical load-displacement curves for progressive end crushing of the intact tube, failure mode I and mode II of the perforated tube (e.g. SC15-1 and SC5-1 in Table 1), respectively. For the intact tube (NH), the axial load increased initially when the loading platen contacted the incident end of tube in the pre-crushing, seen in Fig. 6a. Then the load quickly increased to a peak (i.e. 99.81 kN at 1.86 mm displacement, 100.32 kN at 1.81 mm and 98.52 kN at 1.83 mm for tubes NH-1, NH-2, and NH-3, respectively). After the peak, the load dropped dramatically to a lower and plateau level, in which the crack propagated progressively along the longitudinal axis of the tubes, leading to a steady load fluctuation. The progressive crushing behavior can be characterized by the mean load, representing the overall capacity of buckling resistance to quasi-static compression. The mean load of specimens was relatively stable during the entire crushing process as listed in Fig. 6a and Table 1.

Fig. 6b plots the load-displacement curve for the perforated tube with mode I failure, which can be divided into three distinct regions, defined as pre-crushing, sliding of the fractured tube and secondary loading peak, respectively. It is interesting to note that the peak load in this failure mode varied from 74 kN to 97 kN at an average pre-crushing distance of 1.5 mm, which was much lower than that in the progressive end crushing mode (around 100 kN for the NH specimens in Table 1), indicating the considerable reduction in load bearing capacity. Then the upper half of the tube started penetrating into the lower half, following by a low and stable load until the displacement reached around 50 mm. In the third stage, the resistant load increased rapidly to a second peak, which was around 20–30 kN higher than the first peak. At the third stage the load dropped and then increased dramatically attributable to the complex fracture mechanism as discussed before (Fig. 4c).

Fig. 6c plots the load-displacement curve for the perforated tube with mode II failure, which can be also distinguished into three stages of deformation, namely pre-crushing, local buckling and progressive crushing, respectively. In the pre-crushing stage, the applied load increased rapidly after the loading platen firmly contacted the incident end of tube and reached a peak (i.e. 94.93 kN at 1.71 mm, 98.46 kN at 1.41 mm and 92.99 kN at 1.21 mm for SC5-1, SC5-2, and SC10-1 tubes, respectively). After the peak load, the load dropped dramatically to a lower and a plateau level (only 15% of the peak load approximately). As the deformation proceeded further, local buckling occurred due to fracture of the matrix and reinforced fiber in the tubular shell, causing extensive unstable splitting of the tube wall. After this, the load increased to around 50% of the peak load and established a new plateau with a fairly stable fluctuation, observing the progressive folding in the lower CFRP half.

3.3. Effect of perforation on crushing characteristics

Table 1 summarized the test results, including peak load, mean load and specific energy absorption (SEA). The specific energy absorption is a common yet effective criterion to assess the crashworthiness of structures [30], which is defined as the energy absorption per unit mass of the crushed structure, and calculated as

$$\mathrm{SEA} = \frac{\int_0^d F(x)dx}{\rho A l} \tag{1}$$

where F and d denote the compressive force, crushing displacement respectively; ρ is the average density of the structure material, A is cross section area and l is the length of the crushed tube [39,40]. The detailed discussions are given as below.

3.3.1. Effect of hole size

In order to explore the effect of hole size on the load bearing capacity and energy absorption, eighteen specimens with a single hole of 5, 10, 15, 20, 25 and 30 mm in diameter were tested (three specimens for each diameter), respectively; and the test results were summarized in Table 1 and plotted in Fig. 7. It is observed that the peak load decreased from 97 kN to 78 kN with the increase in the hole diameter, which was around 97.3–78.2% of that from the intact tube. The results implied that the peak load of perforated tubes was not sensitive to hole sizes as the reduction in strength of perforated tubes was less significant than that in perforated composite laminates whose strength could be decreased by 35–70% in presence of a hole [7]. The reason might reside in the fact that the other three tubal walls without perforation would still withstand considerable load under compression, whereas the cutouts in the perforated wall made the panels more vulnerable structurally and easier to buckle and fracture completely. From the tabulated test results and crash failure graphs (Figs. 4 and 5), it is found that the peak load was less significantly dependent on the open hole with a small size (i.e. 5 and 10 mm in diameter here). On the other hand, the dependence of peak load on the open hole was significant for perforated tubes with a great size (diameter bigger than 10 mm) when failure mode I occurred.

As shown in Fig. 7, the reduction in SEA appears more interesting. In presence of a hole, the SEA dropped sharply from 82 kJ/kg to

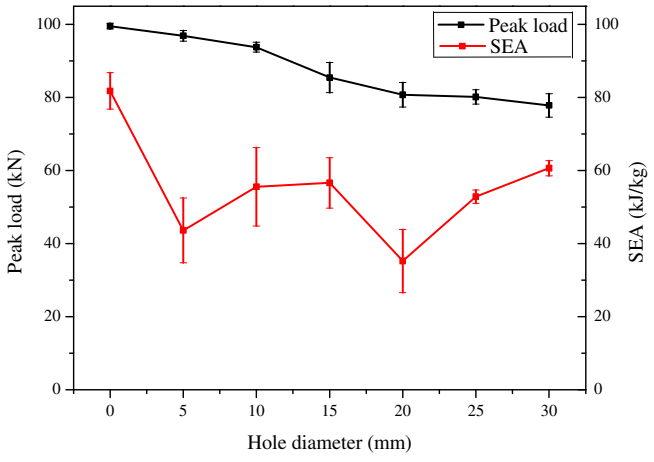

Fig. 7. Effect of hole size on the peak load and SEA of the tested tubes.

44 kJ/kg, reducing by approximately 46.7%, which was mainly due to the difference between the progressive end crushing and unstable failure modes as discussed previously. Nevertheless, the average SEA was seen to vary irregularly when the diameter of hole changed from 5 mm to 30 mm, fluctuating in between 35 and 61 kJ/kg, indicating a more complex failure mechanism when perforation was introduced to tube wall. Importantly, despite the reduction, SEA of the perforated CFRP tube was still higher than that of those intact metallic tubes (approximate 10 kJ/kg) [41,42]. The test results indicated that the SEA of perforated CFRP tubes was appreciably dependent on the presence of open hole. In other words, the SEA was again not sensitive to the hole size, as the capability of energy absorption was mainly determined by the failure mode of perforated tubes. Further studies on structural crashworthiness optimization may be needed in the future to enhance the energy absorbing capacity of the perforated CFRP tubes [43].

The effect of hole size on failure strength of CFRP tube was analyzed by the simple hole-insensitive and hole-sensitive failure criteria proposed by Mikulas [44] for perforated laminates (i.e. [12,45]). If the material is ideally hole-insensitive, the failure strength is proportional to net sectional area. But if the material is hole-sensitive, the specimen fails when the local stress at the hole edge exceeds the strength of the material. As shown in Fig. 8, the data points in the test are above the hole-sensitive curve, which agrees with the testing results of laminates, indicating that the material is not ideally brittle and some load redistribution does take place around the hole [8]. σ_{nh} and σ_h represent the failure stress based on the cross sectional area of the specimen for intact and perforated square tubes, respectively, estimated as:

$$\sigma = \frac{P_{\max}}{A} \tag{2}$$

where $P_{\max}$ and A represent the peak load and cross section area of tube, respectively.

The examples for investigating the effects of circular holes on the compressive strength of perforated composite laminates (plates) are depicted in Fig. 8. Compared to the perforated laminates, the failure strength of the perforated tubes was relatively insensitive to the hole diameter. It was clear that the normalized failure strength of the perforated tube was decreased by around 3–22% in presence of the hole with ratio D/C ranging from 0.02 to 0.12, indicating a much lower reduction rate compared with the perforated laminates (ranging from 36.4% to 46.6% with approximately the same D/W range, where W represents the width of laminated plate) [7,8,10]. Another interesting finding was the effects of small hole on normalized failure strength. The reduction in the failure strength was less than 6% for the perforated CFRP tubes when the D/C was smaller than 0.04, whereas a similar result of small hole effect for composite plate was found in [10] when D/W was less than 0.2 because the stress concentration near the hole decays to the average stress of the plate in a small distance from the hole edge.

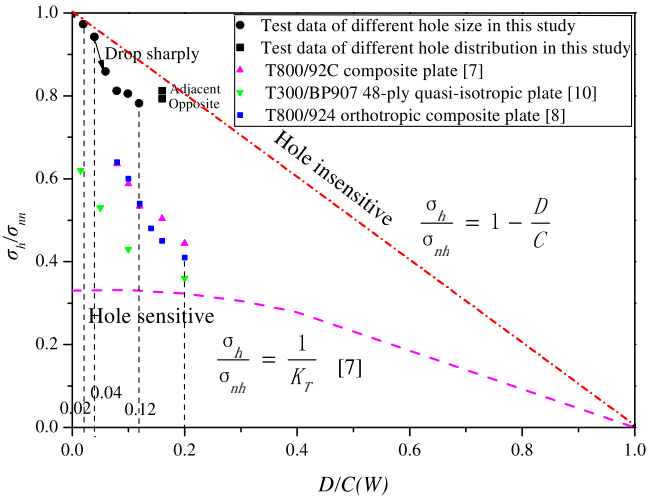

Fig. 8. Effect of hole size on the failure strength of perforated structures.

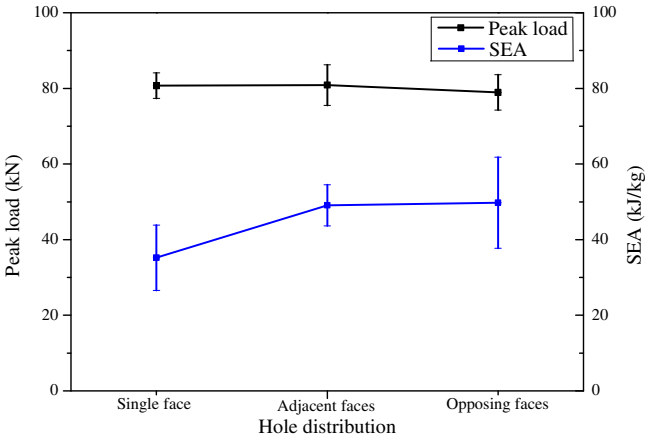

Fig. 10. Effect of hole distribution on crashworthiness performance.

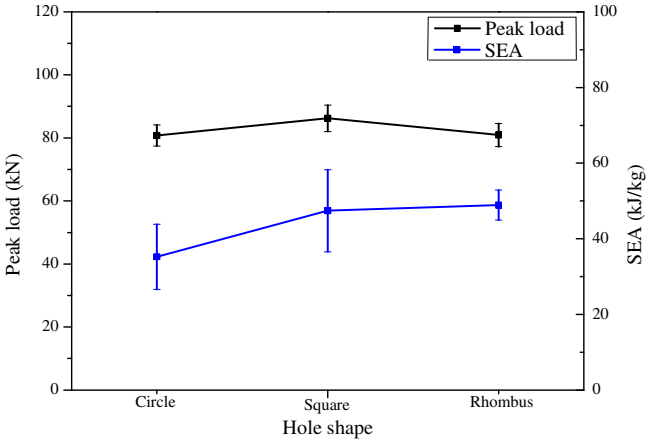

Fig. 9. Effects of hole shape on crashworthiness performance.

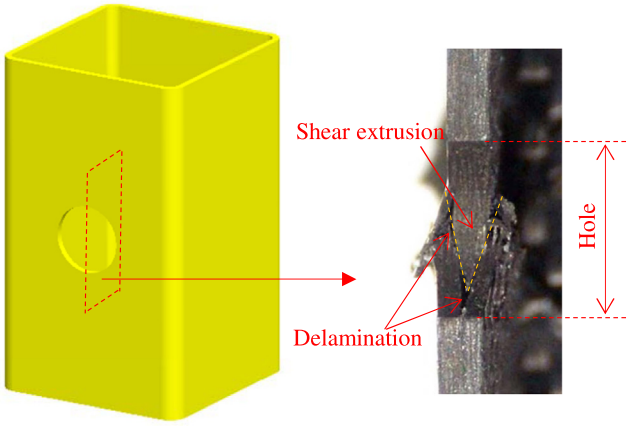

Fig. 11. Cross section of hole area in cracked specimen.

3.3.2. Effect of hole shape

Fig. 9 plots the peak loads and SEA values of the perforated tubes with respect to the hole shapes of circle, square and rhombus, respectively, while keeping the hole area identical. The average peak loads were 80.74, 86.20 and 80.92 kN for the circular, square and rhombus holes, respectively; and the corresponding average SEA values were 35.23, 47.43 and 48.90 kJ/kg respectively. It is interesting to note that the peak load and SEA varied to a certain extent with the different hole shape. The test results showed that the peak load of the perforated CFRP square tubes was not very sensitive to the hole shape. The data indicated that the specimens with square hole had the highest peak load. In the study for the composite plates, however, the results were quite different, the ultimate failure loads of the plate with circular hole under combined action of uniaxial compression and in-plane shear loads were approximately 111.7% and 221.7% of the plate with square and rhombus cutouts, respectively, which was mostly attributable to a relatively lower stress concentration in a circular hole [16]. Our study revealed that the hole shape was insensitive to the load bearing capacity, but was of certain effect on SEA. The SEA of specimens with circular hole was less than 70% of that of the specimens with the square and rhombus hole, which might be attributable to the different failure processes with varying complexity when the upper half of tube penetrated into the lower half in the latter stage of failure mode I (as discussed in Section 3.1).

3.3.3. Effect of hole distribution

Multiple holes were often required on different walls of the composite structures. Three typical distribution patterns of circular holes, namely single face, adjacent faces and opposite faces were considered herein (Fig. 2c). Fig. 10 plots the effect of the hole distribution on the peak load and SEA. It is interesting to note that despite different nominal sectional area with *D/C* of 0.083, 0.167 and 0.167 for single, adjacent and opposite perforated faces respectively, the corresponding peak loads were 80.74, 80.89 and 78.93 kN respectively, within a standard deviation of 0.89 (1.1%); and the corresponding SEA values were 35.23, 49.09 and 49.79 kJ/kg respectively, within a standard deviation of 6.70 (15.0%). The reason why the peak force remained almost constant might pertain to the basic mechanics, where the collapse occurred when the peak stress on the hole edge reached the material strength to crack. Thus the cutouts at different tube walls were of limited influence on each other. Nevertheless, the SEA was found to be associated with the number of holes but not the distribution.

Failure strengths of the tubes with perforation in the adjacent faces and opposite faces are depicted in Fig. 8 (black square point). It can be inferred that increase in number of perforation holes around transverse direction of the tube led to a slight decrease in the peak load of perforated CFRP tube. The results were somewhat different from the perforated GFRP circular tubes reported by Wang et al. [26], where a significant decrease in the axial stiffness was found by increasing the number of holes around the transverse direction. It implied that the effect of hole distribution on the load bearing capacity of perforated tube might be related to both the material and geometric shape of tube.

3.4. Damage mechanism

In order to further understand the damage mechanism of perforated CFRP tubes, the crack initiation, strain distributions and crack propagation around the hole edges were analyzed. An attempt was first made to understand the mechanism of failure initiation by observing the section of hole area. The destructive testing of the perforated tube SC20-4 was interrupted when there was a significant drop of the compressive load; and the cross section of specimen was cut from the middle hole using the high speed computer numerical controlled milling machine, as shown in Fig. 11.

Similar to the damage mechanism of composite laminates as studied in [6–8,10,23], the damage appeared to be initiated through fiber micro-buckling in a direction where transverse stiffness was minimal; then the shear-crippling followed which would produce high shear strains and further damage in the adjacent off-axis plies, thereby causing delamination between the layers [46]. As shown in Fig. 11, significant delamination can be observed inside the hole mostly caused by the increase in the shear stress.

The variation of local strains was further analyzed by investigating the strain distributions at representative locations for perforated CFRP tube SC20-1. As shown in Fig. 12, three strain gauges measuring the axial strains were distributed evenly at region A next to the hole and two strain gauges measuring the transverse strains were distributed evenly at region B. Fig. 12b plots the distribution of tested axial and transverse strains, in which two interesting findings were obtained. First, the axial strain was higher than the transverse strain at the same position around the hole, for example, the axial strain at strain gauge A-3 was around 9 times of transverse strain of B-5, which had the same distance to the edge of hole. Second, the axial strain decreased with the increase in distance from the hole edge (strain at gauge label 3 was higher than

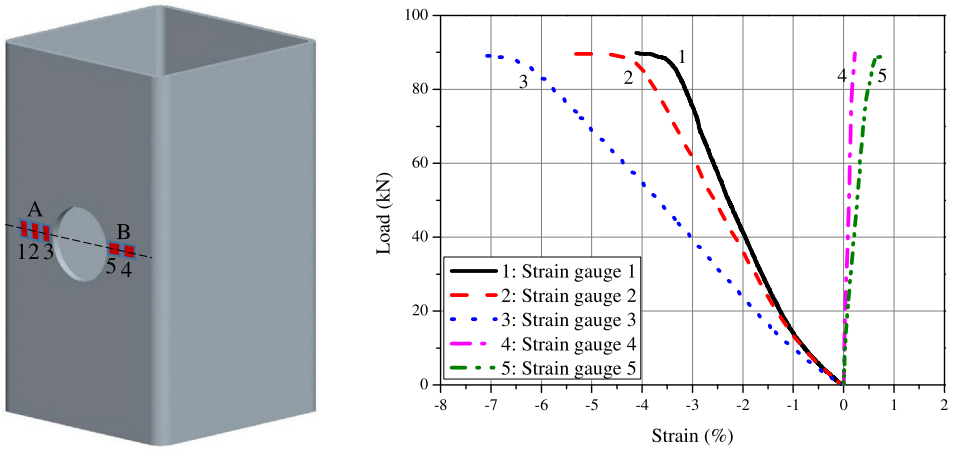

Fig. 12. Strain distributions on tested tubes: (a) strain gauges and (b) tested strains.

those at labels 1 and 2). Therefore, it was evident that the strain/stress concentration did occur around the hole and the significant axial stress led to fiber micro-buckling in the transverse direction of the middle hole edge.

The abovementioned test divulged that the hole damage (interply delamination and fiber microbuckling) was induced mainly by the shear stress/strains under compression. In order to investigate the effect of shear stress which was difficult to quantify experimentally, the finite element analysis was conducted to predict shear stress distribution in the perforation region and further simulate cracking process.

In order to verify the FEA model, Fig. 13 compares the numerical and experimental load-displacement curves of the perforated tube with the single hole of 20 mm in diameter (SC-20), which exhibited good agreement during the whole crushing process. The simulation predicted a slightly earlier initial peak load, with a very close value compared with the testing result (81.27 and 85.22 kN for simulation and experiment, respectively). The FEA generated a relatively lower loading plateau in the second stage. The difference between

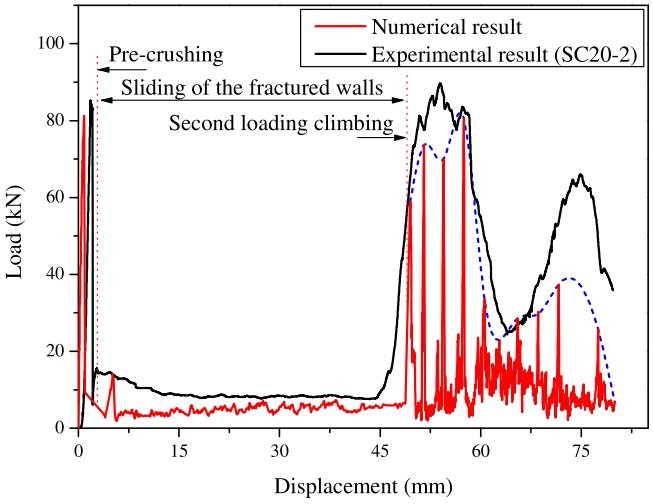

Fig. 13. Comparisons of experimental and numerical load-displacement curves.

the experimental tests and numerical predications was attributed mainly to the underestimation of the frictional interaction of the crushed parts in this stage [47]. The numerical curve fluctuated dramatically during the third region of the crushing process (the secondary loading climb), which was mostly due to deletion of shell elements in the single-layer wall model. This type of modeling technique underestimated the SEA considerably (27.93 J/g and 39.48 J/g for the simulation and experiment, respectively), which was attributed to the fact that the single-layer wall model was unable to precisely simulate the real complex collapses process, such as the inter-laminar failure and frictional interaction of post-fracture [48].

The experimental and numerical crushing processes of SC-20 are compared in Fig. 14. The numerical modeling properly simulated the tube crushing in a form of mid-length collapse mode, where the brittle unstable crack initiated at the hole edge and then propagated circumferentially along the transverse direction, finally splitting the tube in the two halves that penetrated each other as the compressive loading increased. When the two halves contacted to the loading and support platens, few cracks of tubal wall were generated as a result of element deletion in the simulation, which however somewhat differed from the experimental observation with much more complex cracking and bending fronts, From the above comparison, it could be concluded that the established finite element model was effective to model the crushing responses of the perforated composite tubular specimens.

Fig. 15 shows the FEA results of shear stress distribution (at the peak load) around the hole in the perforated tubes with different hole shapes. For the circular hole, the maximum shear stress was around the hole edge at the middle height of the tube; for the rhombus hole, the maximum shear stress occurred around the two corners of the hole perpendicular to the loading direction; and for the square holes, the maximum shear stress arised around the four corners of the hole. In comparison with the experimental results, the location of crack initiation showed very good agreement with the location of the maximum shear stress. It is interesting to note that while the maximum shear stress appeared almost equally at the four corners in the square hole, the two cracks initiates randomly at two corners of the square cutout (the upper two corners, the diagonal corners, and lower two corners, respectively

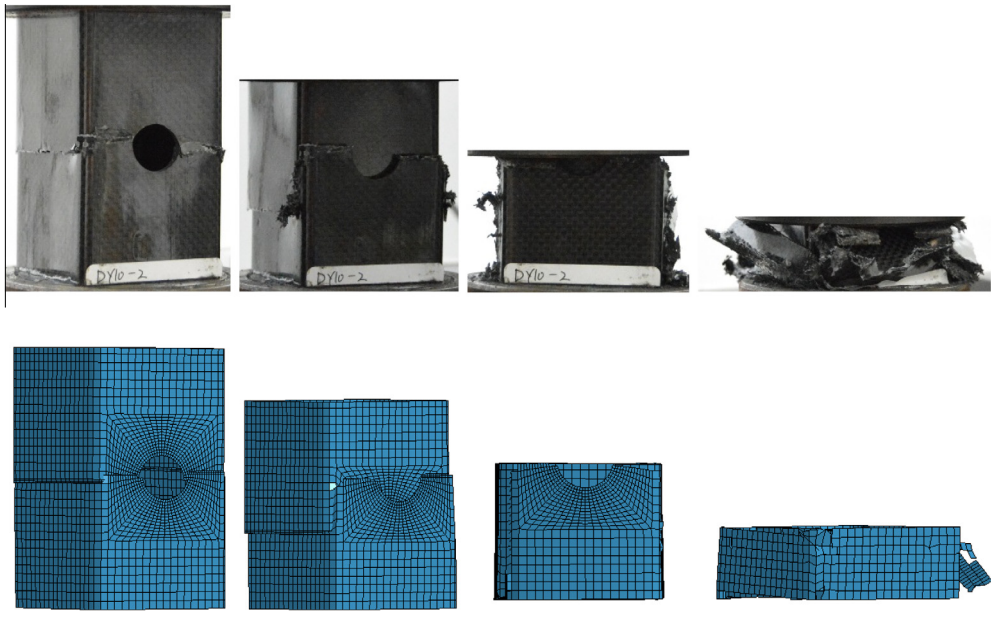

Fig. 14. Comparison of the experimental and numerical crushing processes of SC-20.

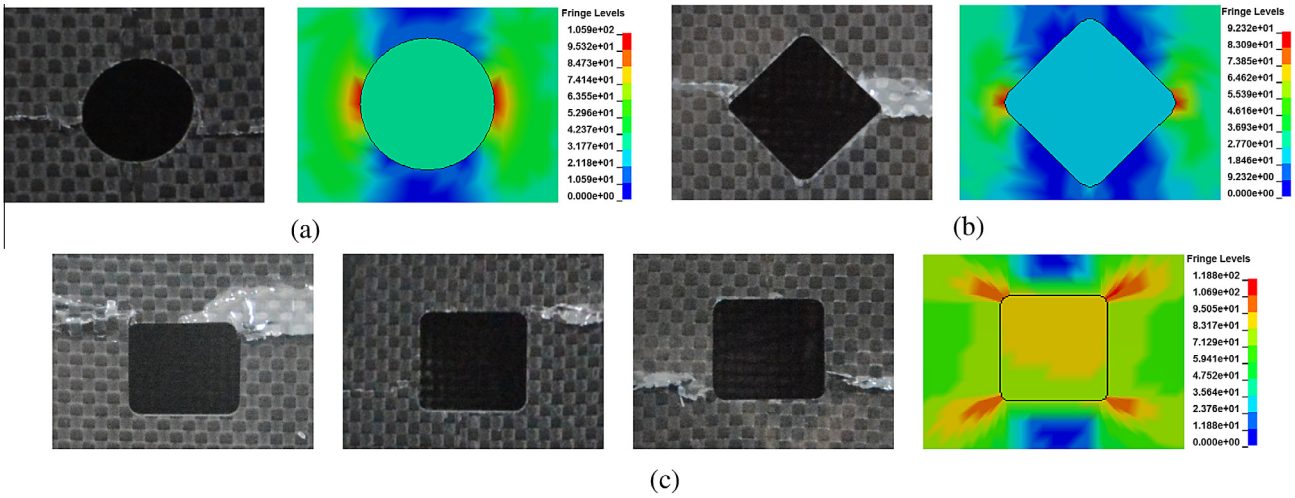

Fig. 15. Numerical and experimental results of crack initiation on perforated tubes: (a) circular, (b) rhombus and (c) square hole.

as in Fig. 15c). The location of crack initiation observed in the perforated CFRP tubes was consistent with the findings by Louhghalam et al. [49] and Yan [50] that all specimens failed from the hole edge and grew perpendicularly to the loading direction. Our finite element analysis results confirmed that there was significant increase in the shear stress around the holes, causing the final mid-height collapse.

Fig. 16 compares the numerical and experimental cracking propagation on the perforated tubes with the circular, rhombus and square holes, respectively. For the tubes with the circular and rhombus holes, the crack initiated from the cutout edge and propagated stably across these four tube walls circumferentially. It is interesting to note that the crack growth rate was nearly the same at the different tube walls until the two cracks met at the

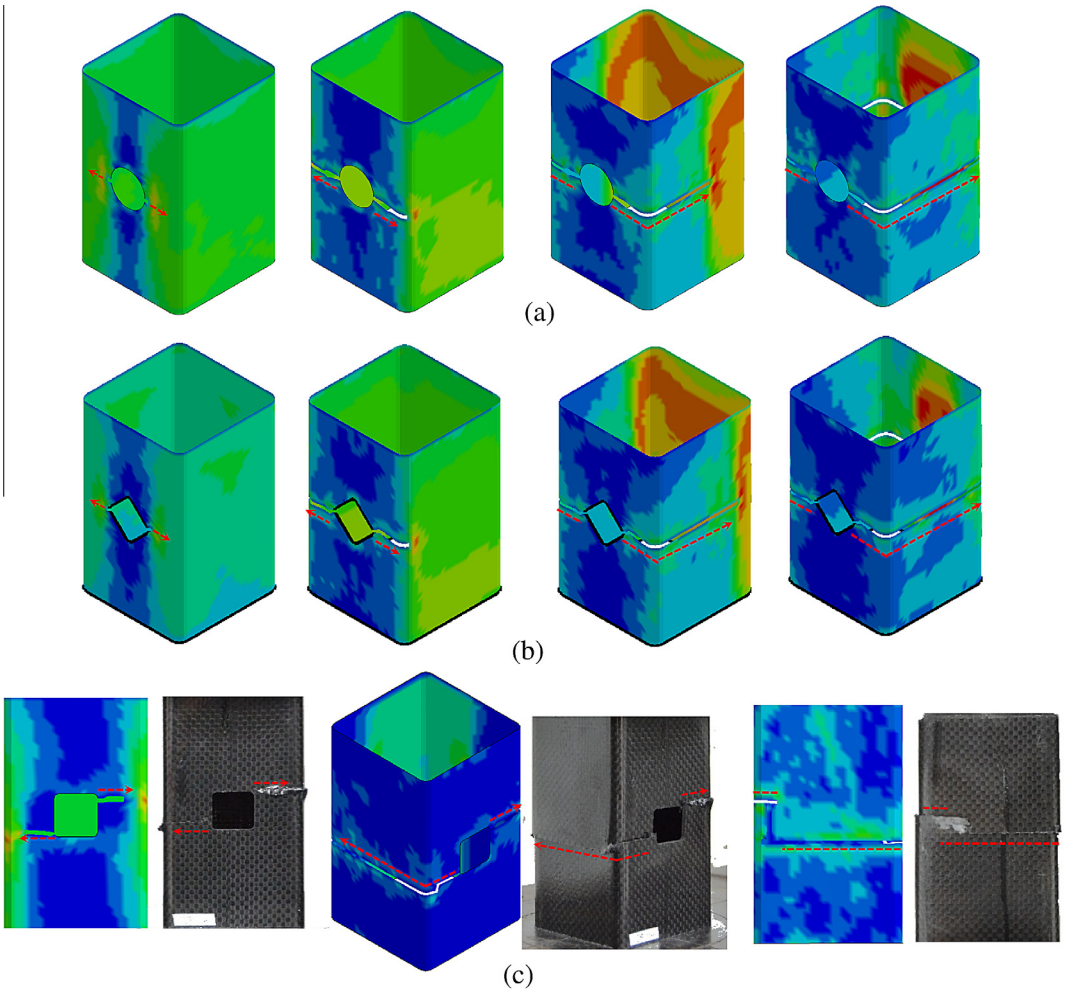

Fig. 16. Crack propagation on perforated tubes: (a) circular, (b) rhombus and (c) square hole.

center of the rear tubal wall. While for the tube with a square hole, the two cracks emanated from diagonal corners of the hole and propagated with different growth rates transversely; then an axial crack appeared and connected the two transverse cracks on the rear tube wall in the end (the 5th sub-figure in Fig. 16c).

4. Conclusions

This paper presented an experimental and numerical study on the failure mechanism and crushing characteristics of perforated square CFRP tubes fabricated by the bladder molding process. The representative load-displacement curves, failure modes and effect of hole size, shape and distribution on compressive behavior of perforated CFRP tubes were investigated. The differences of failure characteristics between the perforated and intact tubes were summarized. The mechanisms of crack initiation and propagation were also analyzed numerically. Within the limitation of the study, the following conclusions can be drawn:

(1) Unlike the progressive crushing observed in the intact CFRP tubes, the mid-height collapse (mode I) and unstable local buckling (mode II) of perforated CFRP tubes were observed in the axial crushing tests, leading to around 3–22% reduction in the first peak force and 26–57% reduction in SEA.
(2) The effect of hole size on failure strength was evaluated by the simple hole-insensitive and hole-sensitive failure criteria. The failure strength of the tube decreased by 3–22% in the presence of the hole, which represented a relatively lower reduction compared to the perforated laminates.
(3) The diameter of circular hole had certain influence on the peak load by decreasing 3–22% when the diameter increased from 5 to 30 mm. Upon presence of hole the SEA dropped sharply from 82 kJ/kg to 44 kJ/kg, but it fluctuated with the increase in the hole size.
(4) The shape and distribution of the hole showed less influence on peak load and SEA compared to the hole size, which were fairly different from the perforated composite laminates. The increase in the number of holes along transverse direction influenced the peak load marginally but SEA considerably.
(5) Both the strain gauges and finite element analysis results exhibited a strong concentrations of shear stress and shear strain around the holes, causing the mid-height collapse of tube. The finite element model was able to closely predict the locations of crack initiation (in the middle two edge for the circular and rhombus holes, two random hole corners for the square hole) and crack propagation on the perforated tubes, which demonstrated satisfactory correlation between the numerical prediction and experimental testing.

Acknowledgements

This investigation was financially supported by the National Natural Science Foundation of China (51675540), the Outstanding Young Scholars of Guangdong Province (2015TQ01X371), the Pearl River S&T Nova Program of Guangzhou (2014J2200005), the Natural Science Foundation of Guangdong Province (2015A030313016), the Natural Science Foundation of Hunan Province (2016JJ3039) and the China Postdoctoral Science Foundation (2015M582323).

References

[1] Liu Q, Mo Z, Wu Y, Ma J, Pong Tsui GC, Hui D. Crush response of CFRP square tube filled with aluminum honeycomb. Compos B Eng 2016;98:406–14.
[2] Liu Q, Lin Y, Zong Z, Sun G, Li Q. Lightweight design of carbon twill weave fabric composite body structure for electric vehicle. Compos Struct 2013;97:231–8.
[3] Rajan VP, Zok FW. Stress distributions in bluntly-notched ceramic composite laminates. Compos A Appl Sci Manuf 2014;60:15–23.
[4] Toubal L, Karama M, Lorrain B. Stress concentration in a circular hole in composite plate. Compos Struct 2005;68:31–6.
[5] Awerbuch J, Madhukar MS. Notched strength of composite laminates: predictions and experiments – a review. J Reinf Plast Compos 1985;4:3–159.
[6] Guynn EG, Bradley WL. A detailed investigation of the micromechanisms of compressive failure in open hole composite laminates. J Compos Mater 1989;23:479–504.
[7] Soutis C, Fleck N, Smith P. Failure prediction technique for compression loaded carbon fibre-epoxy laminate with open holes. J Compos Mater 1991;25:1476–98.
[8] Soutis C, Fleck N. Static compression failure of carbon fibre T800/924C composite plate with a single hole. J Compos Mater 1990;24:536–58.
[9] Soutis C, Curtis P, Fleck N. Compressive failure of notched carbon fibre composites. In: Proceedings of the royal society of London A: mathematical, physical and engineering sciences. The Royal Society; 1993. p. 241–56.
[10] Starnes J. Failure characteristics of graphite-epoxy structural components loaded in compression. Recent Adv Mech Comp Mater; 1983. p. 283–306.
[11] Camanho PP, Maimí P, Dávila CG. Prediction of size effects in notched laminates using continuum damage mechanics. Compos Sci Technol 2007;67:2715–27.
[12] Erçin GH, Camanho PP, Xavier J, Catalanotti G, Mahdi S, Linde P. Size effects on the tensile and compressive failure of notched composite laminates. Compos Struct 2013;96:736–44.
[13] Lee J, Soutis C. Measuring the notched compressive strength of composite laminates: specimen size effects. Compos Sci Technol 2008;68:2359–66.
[14] Hallett SR, Green BG, Jiang WG, Wisnom MR. An experimental and numerical investigation into the damage mechanisms in notched composites. Compos A Appl Sci Manuf 2009;40:613–24.
[15] Rezaeepazhand J, Jafari M. Stress analysis of perforated composite plates. Compos Struct 2005;71:463–8.
[16] Kumar D, Singh SB. Stability and failure of composite laminates with various shaped cutouts under combined in-plane loads. Compos B Eng 2012;43:142–9.
[17] Durelli A, Erickson M, Rajaiah K. Optimum shapes of central holes in square plates subjected to uniaxial uniform load. Int J Solids Struct 1981;17:787–93.
[18] Durelli A, Rajaiah K. Optimum hole shapes in finite plates under uniaxial load. J Appl Mech 1979;46:691–5.
[19] Muc A. Transverse shear effects in shape optimization of thinwalled laminated composite structures. Compos Struct 1995;32:399–408.
[20] Liu Y, Jin F, Li Q. A strength-based multiple cutout optimization in composite plates using fixed grid finite element method. Compos Struct 2006;73:403–12.
[21] Ng S-P, Lau K, Tse P. 3D finite element analysis of tensile notched strength of 2/2 twill weave fabric composites with drilled circular hole. Compos B Eng 2000;31:113–32.
[22] Su ZC, Tay TE, Ridha M, Chen BY. Progressive damage modeling of open-hole composite laminates under compression. Compos Struct 2015;122:507–17.
[23] Wang J, Callus PJ, Bannister MK. Experimental and numerical investigation of the tension and compression strength of un-notched and notched quasi-isotropic laminates. Compos Struct 2004;64:297–306.
[24] Xu W, Thorsson SI, Waas AM. Experimental and numerical study on cross-ply woven textile composite with notches and cracks. Compos Struct 2015;132:816–24.
[25] Taheri-Behrooz F, Esmaeel RA, Taheri F. Response of perforated composite tubes subjected to axial compressive loading. Thin Walled Struct 2012;50:174–81.
[26] Wang W, Sheikh MN, Hadi MNS. Behaviour of perforated GFRP tubes under axial compression. Thin Walled Struct 2015;95:88–100.
[27] Jacob A. Carbon fibre and cars – 2013 in review. Reinf Plast 2014;58:18–9.
[28] Morey B. Carbon fiber on its way? Manuf Eng 2011;147:81–91.
[29] Liu Q, Ma J, Kang L, Sun G, Li Q. An experimental study on fatigue characteristics of CFRP-steel hybrid laminates. Mater Des 2015;88:643–50.
[30] Liu Q, Xing H, Ju Y, Ou Z, Li Q. Quasi-static axial crushing and transverse bending of double hat shaped CFRP tubes. Compos Struct 2014;117:1–11.
[31] Liu Q, Ou Z, Mo Z, Li Q, Qu D. Experimental investigation into dynamic axial impact responses of double hat shaped CFRP tubes. Compos B Eng 2015;79:494–504.
[32] Tan SC. A progressive failure model for composite laminates containing openings. J Compos Mater 1991;25:556–77.
[33] Chang FK, Chang KY. A progressive damage model for laminated composites. J Compos Mater 1987;21:834–55.
[34] Huang J, Wang X. Numerical and experimental investigations on the axial crushing response of composite tubes. Compos Struct 2009;91:222–8.
[35] Feraboli P, Wade B, Deleo F, Rassaian M, Higgins M, Byar A. LS-DYNA MAT54 modeling of the axial crushing of a composite tape sinusoidal specimen. Compos A Appl Sci Manuf 2011;42:1809–25.
[36] Mamalis AG, Manolakos DE, Ioannidis MB, Papapostolou DP. The static and dynamic axial collapse of CFRP square tubes: finite element modeling. Compos Struct 2006;74:213–25.
[37] Ridha M, Wang CH, Chen BY, Tay TE. Modelling complex progressive failure in notched composite laminates with varying sizes and stacking sequences. Compos A Appl Sci Manuf 2014;58:16–23.
[38] Mamalis AG, Manolakos DE, Ioannidis MB, Papapostolou DP. Crashworthy characteristics of axially statically compressed thin-walled square CFRP composite tubes: experimental. Compos Struct 2004;63:347–60.

[39] Joosten MW, Dutton S, Kelly D, Thomson R. Experimental evaluation of the crush energy absorption of triggered composite sandwich panels under quasi-static edgewise compressive loading. Compos A Appl Sci Manuf 2010;41:1099–106.
[40] Pitarresi G, Carruthers JJ, Robinson AM, Torre G, Kenny JM, Ingleton S, et al. A comparative evaluation of crashworthy composite sandwich structures. Compos Struct 2007;78:34–44.
[41] Nia AA, Badnava H, Nejad KF. An experimental investigation on crack effect on the mechanical behavior and energy absorption of thin-walled tubes. Mater Des 2011;32:3594–607.
[42] Yin H, Wen G, Hou S, Chen K. Crushing analysis and multiobjective crashworthiness optimization of honeycomb-filled single and bitubular polygonal tubes. Mater Des 2011;32:4449–60.
[43] Fang J, Sun G, Qiu N, Kim NH, Li Q. On design optimization for structural crashworthiness and its state of the art. Struct Multidiscip Optim 2016:1–29.
[44] Mikulas M. Failure prediction techniques for compression loaded composite laminates with holes. Selected NASA Res in Composite Mater and Struct (SEE N 80-28436 19-24) 1980. P. 1–33.
[45] Camanho PP, Erçin GH, Catalanotti G, Mahdi S, Linde P. A finite fracture mechanics model for the prediction of the open-hole strength of composite laminates. Compos A Appl Sci Manuf 2012;43:1219–25.
[46] Ridha M, Wang CH, Chen BY, Tay TE. Modelling complex progressive failure in notched composite laminates with varying sizes and stacking sequences. Compos A Appl Sci Manuf 2014;58:16–23.
[47] Mamalis AG, Manolakos DE, Ioannidis MB, Papapostolou DP. The static and dynamic axial collapse of CFRP square tubes: finite element modelling. Compos Struct 2006;74:213–25.
[48] Bussadori BP, Schuffenhauer K, Scattina A. Modelling of CFRP crushing structures in explicit crash analysis. Compos B Eng 2014;60:725–35.
[49] Louhghalam A, Igusa T, Park C, Choi S, Kim K. Analysis of stress concentrations in plates with rectangular openings by a combined conformal mapping – finite element approach. Int J Solids Struct 2011;48:1991–2004.
[50] Yan X. Cracks emanating from circular hole or square hole in rectangular plate in tension. Eng Fract Mech 2006;73:1743–54.